Quantitative Simulation of Back Scatter X-ray Imaging and Comparison to Experiments

Gerd-Rüdiger JAENISCH, Sanjeevareddy KOLKOORI, Carsten BELLON
BAM Bundesanstalt für Materialforschung und -prüfung, Berlin, Germany

Contact e-mail: gerd-ruediger.jaenisch@bam.de

Abstract. X-ray backscatter imaging is a well established NDT technique to inspect complex objects using only a single-sided access. In difference to conventional transmission X-ray radiography, the X-ray backscatter imaging utilizes the scattered radiation caused by the Compton scattering effect. In order to achieve high backscatter intensities from a test object, it is necessary to optimize the backscatter system parameters namely the angle between source and slit camera, the slit collimator system, the shielding between source and scatter camera, and the type of detector. In addition, the scatter phenomena in to the investigated object need to be understood.

In this contribution, we present a Monte Carlo model *McRay* which considers all relevant single and multiple interactions of photons and electrons. This model can be used to simulate back scatter techniques. It allows not only calculating the scatter image for a given experimental setup but also registering the spectrum of the detected scattered photons. Both aspects are important to understand the imaging process, to interpret the results, and to optimize the backscatter camera investigated here. Additionally experimental results will be presented and compared with simulations.

1 Introduction

In difference to conventional transmission X-ray radiography and computed tomography (CT), the X-ray backscatter technique utilizes the scattered radiation caused by the Compton scattering effect [1-3]. As the Compton scattering effect depends on the electron density in the scattering object, low-atomic-number Z materials (eg. Al, perspex, composites and water) exhibit predominant scattered radiation compared to the heavy metals such as steel (Fe), copper (Cu), and lead (Pb), respectively. The efficiency of the X-ray backscatter technique depends on how accurate and fast the scattered radiation from the object is collected on the detector using only a single-sided access.

ComScan, a commercially available X-ray backscatter imaging system for NDT of aerospace components, was presented by Harding et al. [4]. Here, the backscatter image is visualized using a finely collimated X-ray source (160 kV) and a detector array equipped with slit collimators. Furthermore, ComScan visualizes 22 planes in different depths in one scan using a flying-spot arrangement for the X-ray beam. The main disadvantages are the reduced beam opening and collimated X-ray source resulting in a poor signal-to-noise ratio (SNR) and a long measurement time.

The AS&E flying-spot X-ray backscatter technique uses a highly collimated beam of X-rays and large area detectors for collecting backscatter X-rays from the inspected ob-

ject [5]. The main limitations of this technique are the fixed irradiation geometry and a single-viewing direction. This imaging technique has been employed for security applications to detect thereat and contraband materials in large containers, vehicles, and baggage [6].

A pinhole camera based X-ray backscatter imaging technique uses an uncollimated powerful X-ray source along with an efficient camera encompassed with a digital detector array for the backscatter imaging of a test-object. This X-ray backscatter camera is also equipped with a novel twisted slit collimator [7-9].

Compton backscatter imaging for corrosion detection in thick metals using gamma rays were reported [10] where the scattered radiation was measured using a collimated gamma ray beam and scintillation detectors. Generally, gamma ray backscatter techniques are not suitable for NDT of aerospace materials because of the heavy shielding required for radioactive sources, low spatial resolution images and large scanning time (in the order of hours). A review on X-ray backscatter imaging methods for nondestructive testing and evaluation was presented by Niemann et al. [11]. In addition, the X-ray backscatter technology was successfully applied in medical and security fields [12,13].

In order to optimize the X-ray backscatter system design (e.g. collimator) and parameters (angle between source, detector, and sample surface), Monte Carlo simulation tools [14-16] were used. These software tools have been employed to simulate several backscatter detection modes such as flying-spot arrangement with large area detectors, imaging using photon counting detectors, and evaluating scattered spectra. A CAD based backscatter simulation code for virtual inspection of an object with single side access was earlier presented by Gray et al. [17].

In this work, a Monte Carlo code called *McRay* [18,19] together with the simulator *aRTist* [20,21] is presented to simulate X-ray backscatter techniques for single side imaging of material defects. First, the X-ray backscatter imaging principle, a short discussion on the developed X-ray backscatter camera [22], and the investigated test specimen are presented. Then, the backscatter simulation using the Monte Carlo method along with multiple photons tracing scenarios are illustrated. Finally, the simulation results are compared to experiments and reasons for discrepancies are discussed.

2 X-Ray Backscatter Imaging Technique

The X-ray backscatter technique presented in this work uses uncollimated X-ray radiation to irradiate the whole object being inspected. It uses a combination of a twisted slit collimator and a digital detector array (DDA) to image backscattered radiation. Fig. 1 shows schematic this X-ray backscatter technique for nondestructive imaging of materials. In the following, a detailed description of the twisted slit collimator and the construction of the X-ray backscatter camera are discussed.

2.1 Twisted Slit Collimator

Fig. 2(a) shows schematic the twisted slit collimator. The inside of the slit is lined with ruled surfaces. Consequently, the linear passage of the backscatter radiation through the slit is possible only through a hole-shaped gap [7,22]. The scheme of the twisted slit collimator with dimensions of 50×50 mm^2 is shown in Fig. 2(b). The slit collimator is made from tungsten for high-energy applications. On the front side, the slit is inclined into one direction and on the backside it is inclined in the opposite direction. This approach results in a large angular aperture with a wall thickness adequate for shielding high energy X-ray radiation (>1 MeV) that passes the slit-collimator.

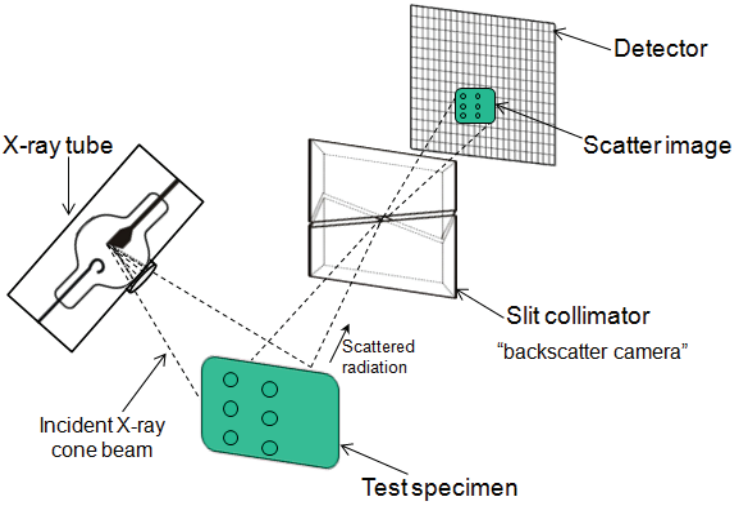

Fig. 1. Schematic presentation of an X-ray backscatter technique using an uncollimated incident X-ray beam and an efficient pinhole camera with a DDA.

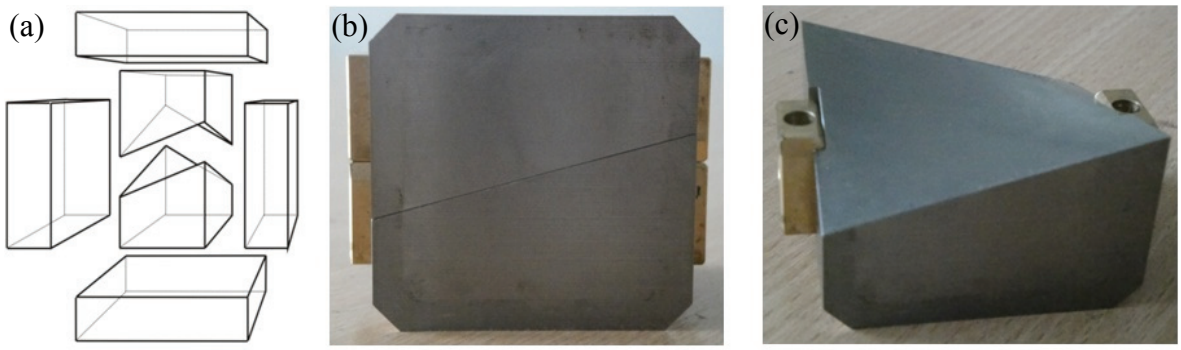

Fig. 2. (a) Schematic diagram of the twisted slit collimator for backscatter imaging, (b) photograph of the constructed slit, and (c) the geometry of the lower part of the slit collimator showing the ruled surface.

2.2 Construction of the X-ray Backscatter Camera

Fig. 3 shows the developed portable X-ray backscatter camera for nondestructive testing (NDT). The two ends of the slit collimator are equipped with a spring loaded system for controlling the passage of backscattered X-ray beam by adjusting the gap between upper and lower part of the collimator. At the same time the resolution in the X-ray backscatter image can be controlled by varying the slit width of the camera (see Fig. 3(a)). Fig. 3(b) shows the internal construction of the backscatter camera. Furthermore, by varying the distance between the collimator and the DDA, the magnification in a backscatter image can be optimized. Apart from that, the present design of the X-ray backscattering camera requires some additional lead shielding in order to avoid undesired scattered radiation and to protect the detector electronics.

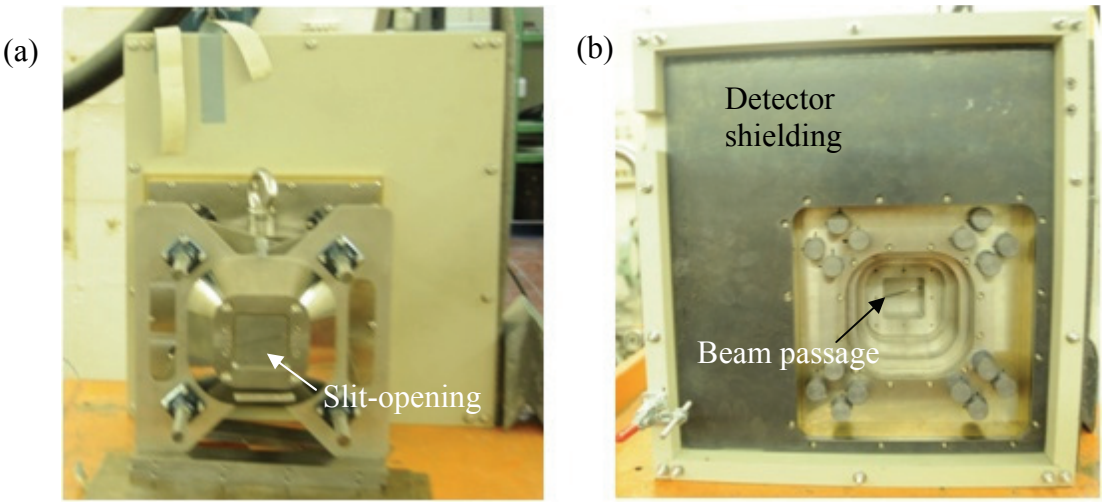

Fig. 3. The constructed mobile X-ray backscatter camera: (a) front view and (b) internal construction of the camera. The camera has a weight of 50 kg. The slit width can be varied between 0.1 mm and 2 mm.

3 Experimental Setup and Data Acquisition

The experimental setup used for X-ray backscatter imaging of a test object is shown in Fig. 4. In this work, a high-power X-ray source (GE ISOVOLT Titan E) with a maximum tube voltage of 420 kV and the anode current of 10 mA is used. The target of the X-ray tube is made of tungsten, with 7 mm thick beryllium window. The focal spot size is about 2 mm. The X-ray backscatter camera is placed close to the X-ray source forming an angle of about 45° between the incident and the scattered X-ray beam for imaging (see Fig. 4). For the experiments a slit width of 50 µm is used. The backscattered X-ray signals are measured using a matrix detector (VIDISCO Rayzor-XPro) with a detection area of 22.2×22.2 cm^2 and 1560×1560 pixels with a size of 143 µm. The scintillator material is amorphous silicon. For the data acquisition the ISee-professional software [23] is used. In order to shield the matrix detector against undesired direct radiation from the X-ray source and the scatter radiation from surrounding objects, additionally 5 mm thick lead plates between the X-ray source and the detector, and also around the slit collimator (Fig. 4) are placed. In the present experimental investigation, the exposure time to obtain one X-ray backscattering image is 10 minutes.

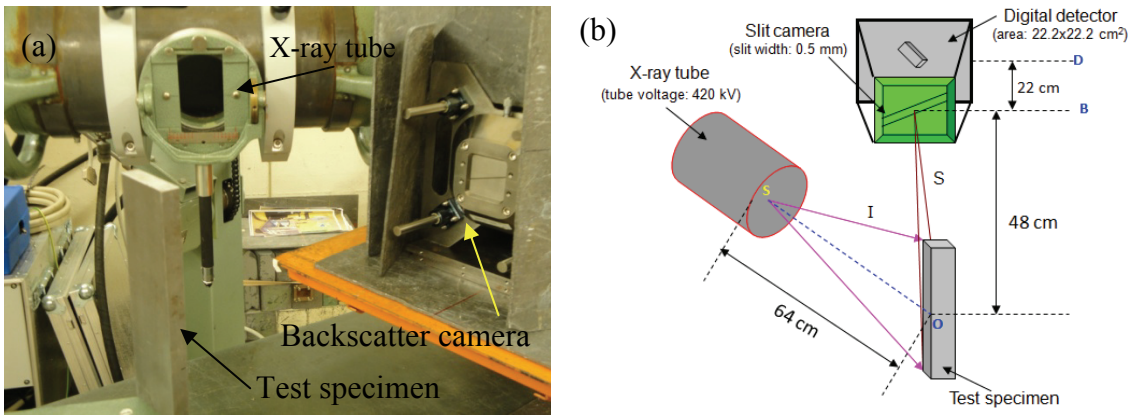

Fig. 4. (a) Photograph of the experimental setup used for the X-ray backscatter imaging of a test object and (b) schematic of the setup showing quantitative geometrical parameters.

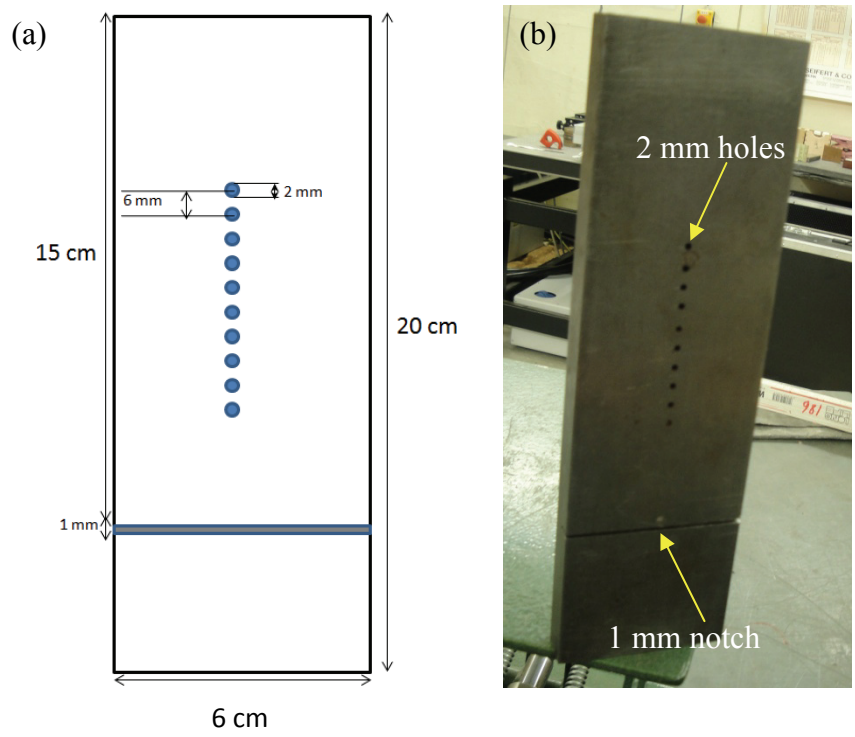

Fig. 5. (a) Schematic of the test specimen used for the backscatter investigation and (b) photograph of the 16 mm thick steel test specimen showing holes with 2 mm diameter and a notch of 1 mm width. The depth of holes varies between 1 mm and 10 mm. The depth of notch is 8.5 mm.

The scheme of the test specimen is shown in Fig. 5. The test specimen consists of 16 mm thick ferritic steel. The steel specimen contains 10 equally spaced flat bottom holes with a diameter of 2 mm at different depths. The depth of holes varies between 1 mm and 10 mm. In addition, it consists of a notch of 1 mm width and 8.5 mm depth. The photograph of the test specimen is shown in Fig. 5(b).

4 Backscatter Simulation Using *aRTist* and *McRay*

4.1 Theory

Modelling of radiation techniques basically consist of four components: (*i*) the radiation source, (*ii*) the interaction of radiation with material, (iii) the detection of the radiation, and (*iv*) the geometry of object under investigation.

X-rays are usually produced by the deceleration of high-energy electrons impinging on a metallic target. X-rays for most practical applications are generated in X-ray tubes, which consist of a cathode and an anode made from heavy metal with high melting point. Electrons are emitted from the cathode and accelerated to the anode in a high-voltage electrical field. When the electrons hit the target of the X-ray tube the energy is transformed in several ways yielding the production of: (*i*) Bremsstrahlung with a continuous spectrum, (*ii*) characteristic radiation, and (*iii*) for most of the energy heat. The implemented model is described in detail in [24].

For the interaction of radiation with material the model is here restricted to photon interactions and do not account for electrons, which are also implemented in *McRay*. Accordingly the following interaction mechanisms are considered: the photoelectric effect, coherent and incoherent scattering, and for photon energies larger than 1 MeV pair production. To account for electron binding effects form factors and scattering functions are used

for coherent and incoherent scattering. Additionally secondary effects such as X-ray fluorescence are considered.

The stationary Boltzmann equation (1) is used to model the photon transport

$$\boldsymbol{\Omega}\cdot\nabla I\left(\boldsymbol{r},E,\boldsymbol{\Omega}\right)+\mu\left(E\right)I\left(\boldsymbol{r},E,\boldsymbol{\Omega}\right)= \int_0^\infty \mathrm{d}E'\int_{4\pi}\mathrm{d}\Omega'\;\sigma\left(E'\rightarrow E,\boldsymbol{\Omega}'\rightarrow\boldsymbol{\Omega}\right)I\left(\boldsymbol{r},E',\boldsymbol{\Omega}'\right)+S\left(\boldsymbol{r},E,\boldsymbol{\Omega}\right). \tag{1}$$

It describes the variation of the photon flux $I(\boldsymbol{r},E,\boldsymbol{\Omega})$ at position $\boldsymbol{r}$ with direction $\boldsymbol{\Omega}$ and energy E. The left hand side of Eq. (1) accounts for the reduction of the flux by the interaction of photons with matter given by the linear attenuation coefficient $\mu(E)$

$$\mu\left(E\right)=\tau+\sigma_{\text{coherent}}+\sigma_{\text{incoherent}}+\pi \tag{2}$$

with the absorption coefficient τ, the scattering coefficients σ_{coherent} and $\sigma_{\text{incoherent}}$, and the pair production coefficient π. The right hand side describes the increase of the photon flux $I(\boldsymbol{r},E,\boldsymbol{\Omega})$ by scattering contributions from other energies E' and other directions $\boldsymbol{\Omega}'$ given by the scattering cross section $\sigma(E'\rightarrow E,\boldsymbol{\Omega}'\rightarrow\boldsymbol{\Omega})$ as well as by internal photon sources $S(\boldsymbol{r},E,\boldsymbol{\Omega})$ such as X-ray fluorescence or electron-positron annihilation.

Eq. 1 is solved by means of the Monte Carlo method. As Monte Carlo calculations for complex geometries commonly demand extensive computational efforts, *McRay* has been developed for linkage to *aRTist* serving as graphical user interface. For a more detailed description of the scatter contribution the *McRay* calculation can be very time consuming.

Calculated or measured transmission functions are used in order to describe the conversion of photons registered by the detector and its response. The energy dependence of the response of a specific detector is included. The inner unsharpness is simulated by Gaussian filtering. Noise is added to the image pixel by pixel depending on its grey value.

aRTist models a real inspection scenario by defining a virtual setup. Source and detector consist of raster points on a finite extended plane. Besides source and detector the geometrical computer model of the experimental setup has to support the representation of the test sample geometry. One or more geometrical part representations can be freely arranged in virtual scene. Parts are described by a boundary representation of closed surfaces, which separate areas of homogeneous material. A facetted (triangulated) boundary description is used in *aRTist*. Curved boundaries are approximated by an appropriate number of plane facets. For data exchange of this facetted part description the STL format is used, which is a de-facto standard in the CAD domain. Several, interactive arrangeable parts can easily be managed in the virtual 3D scene. Overlap of geometries in the scene and combination by Boolean operators leads to variable defect descriptions independent from the surrounding host material of the defect. The inspection scenario defined in *aRTist* is sent to *McRay* for performing the Monte Carlo calculations.

4.2 Simulation Setup using aRTist and McRay

As the Monte Carlo model considers all relevant interactions of photons and electrons, *McRay* can be used to simulate back scatter techniques. In this case *aRTist* is utilized as graphical user interface for *McRay*. In addition to the interactive composition of the experimental setup, the examination of the resulting images and spectra can also be done with *aRTist*. Because *McRay* has been specifically developed for radiographic testing simulation

and is not optimized for backscatter techniques, it is recommended to be executed on a remote system (e.g. HPC cluster or hardware allowing parallel computing).

Fig 6 shows the simulation setup for back scatter imaging (compare Fig. 4(b)) with the described specimen in Fig. 5 created in *aRTist*. On the right hand side of Fig. 6 three orthogonal views of the scene are shown to support the reader in its 3D imagination of the setup. To be comparable with the experimental results, the X-ray spectrum was calculated for a kilovoltage of 420 kV considering a 7 mm thick beryllium window. As in the experiments the slit width was chosen to be 500 µm. The same size of 22.2×22.2 cm^2 for the detection area was used. Due to statistics for the Monte Carlo simulation the calculated image consist of 888×888 pixels with a pixel size of 250 µm.

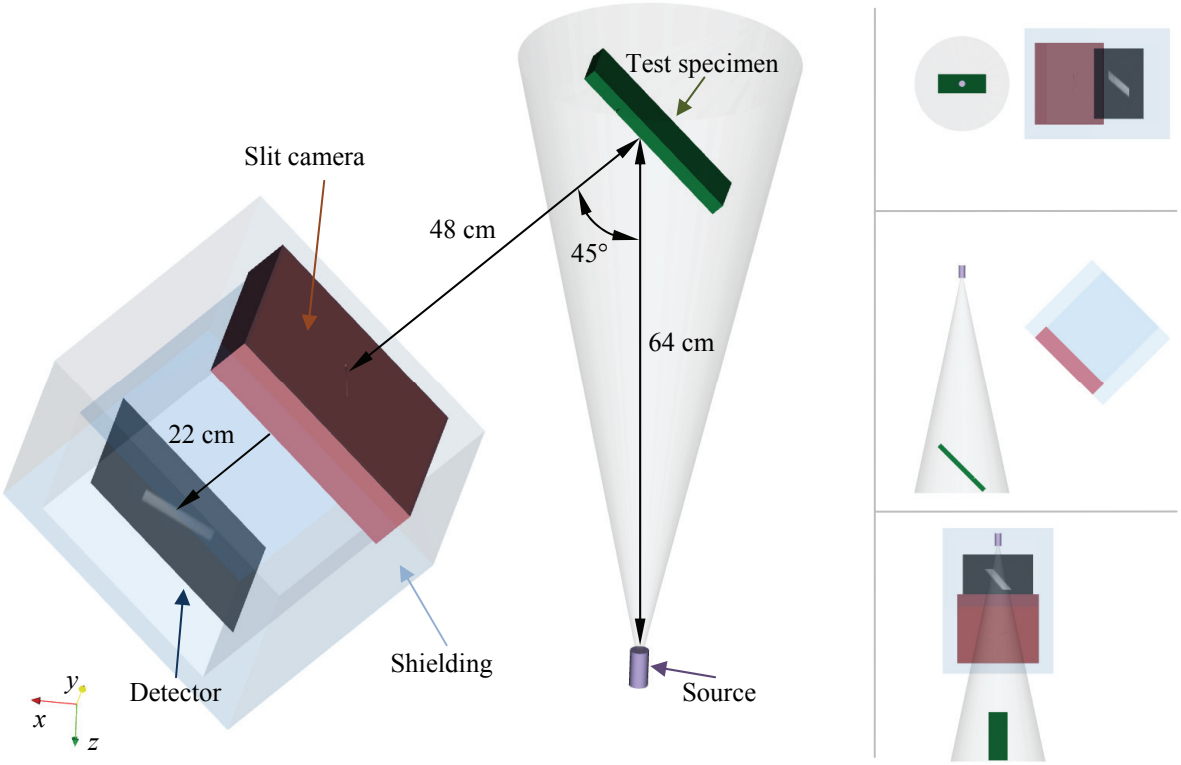

Fig. 6. *aRTist* virtual scene showing the simulation setup.

4.3 Simulation Results

To illustrate the contribution to the back scatter image, Fig. 7 visualizes selected photon traces hitting the detector from the Monte Carlo simulation with *McRay*. As in Fig. 6 three orthogonal views are shown on the right hand side. Here different setups for shielding the detector are presented. In case of no shielding (Fig. 7(a)) most contributions to the detections come from scattering in air at the source side. When shielding this side with lead, still a considerable contribution from scattering in air is obtained. Only if the detector is fully shielded (Fig. 7(c)) scattering in air is negligible.

Fig. 8 shows selected traces inside the specimen to demonstrate combinations of different attenuation mechanisms in a detailed view. Multiple scatter is clearly visible as well as scattering followed by an absorptions event.

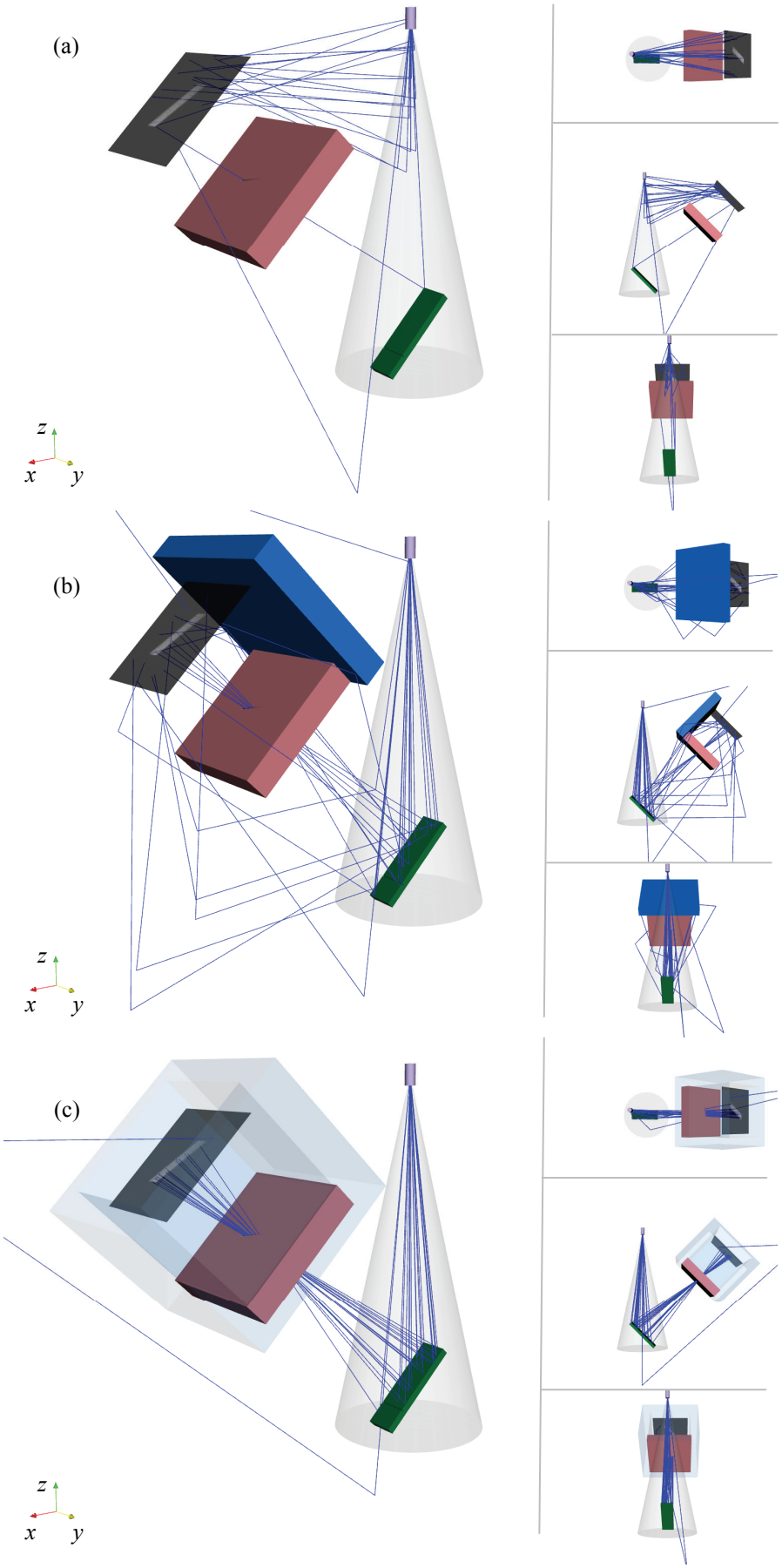

Fig. 7. Visualization of selected traces hitting the detector for various setups: (a) no shielding, (b) single side shielding, and (c) full shielding of the detector.

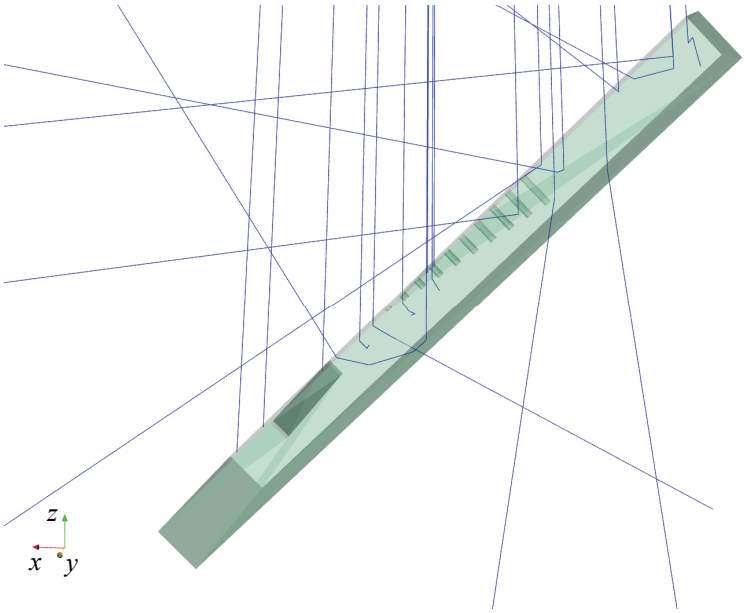

Fig. 8. Detailed visualization of selected traces inside the specimen depicted in a transparent mode.

5 Comparison between Simulation and Experiment

Fig. 9(a)-(d) shows the comparison of the experimental and simulated results for the above described back scatter setup. Fig. 9(a) and (c) present the experimental and simulated scatter images, respectively, while Fig. 9(b) and (d) show the corresponding profiles. The experimental results show clear indications of the notch as well as of the 10 flat bottom holes. The holes do not appear as circles because of the 45° angle between the incident beam and the scatter camera. The SNR is about 100 in the experimental data.

In the simulation the SNR is about 20 after tracing 8×10^{13} photons. Also here a indication of the notch can be seen. This indication is about two times broader than in the experimental results. Remember, the detector used for the experiment has a pixel size of 143 µm while for the simulation a pixel size of 250 µm was chosen which explains the larger unsharpness in the simulation. Due to the poor SNR no indications of the flat bottom holes were found. To achieve the same SNR as in the experiment the number of traced photons has to be increased by a factor of about 25 which has not been done on the available hardware due to the computational expenses.

6 Conclusions

An X-ray backscatter imaging technique has been presented making use of a specially designed twisted slit scatter camera. After discussing the principles of the X-ray backscatter technique the experimental setup and data acquisition was presented. In order to achieve high backscatter intensities from a test object, it is necessary to optimize the backscatter system parameters namely the angle between source and slit camera, the slit-collimator system, the shielding between the source and the scatter camera, and the type of detector. In order to achieve this goal a Monte Carlo model for simulating the back scatter technique has been presented. This model is capable to describe all relevant interactions of photons and electrons with matter. Additionally secondary effects such as X-ray fluorescence and Bremsstrahlung production are included in the model. For the investigation presented here only photon interactions have been considered including X-ray fluorescence while electron

transport has been neglected. The used model is capable to simulate arbitrary experimental setups defined by a virtual scene.

Experimental and simulation results have been presented and compared. The experimental results have shown indications from all features in the chosen specimen while the simulation did not contain information about the flat bottom holes present in the specimen. Possible reasons for this have been discussed.

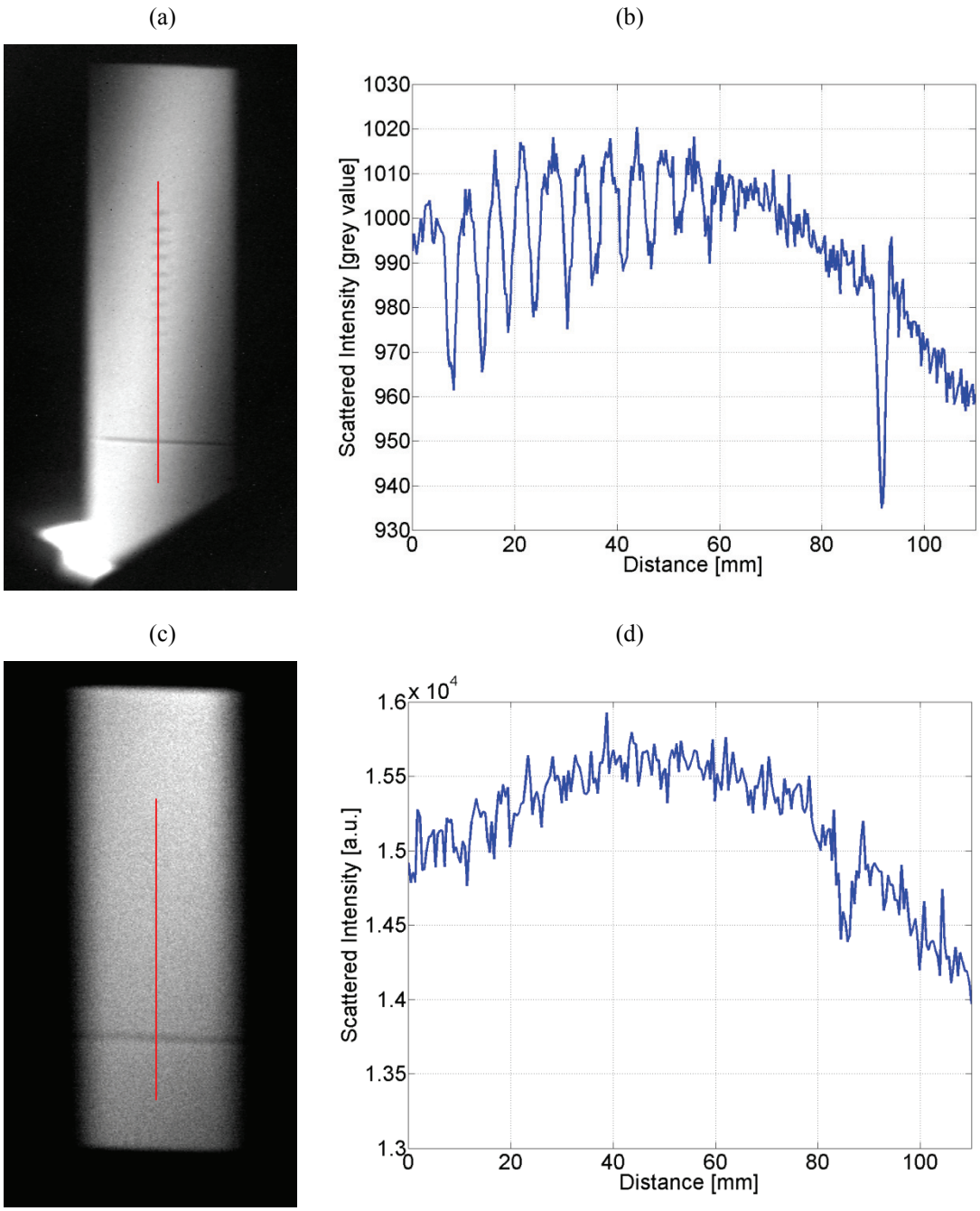

Fig. 9. Quantitative comparison of scattered intensities obtained by the experiment and the *McRay* simulation: (a) experimental scatter image, (b) profile as indicated by the red line, (c) and (d) as (a) and (b) but simulated.

References

[1] W. Heitler, 'The quantum theory of radiation', 3rd ed., Oxford University Press: London, 1954.

[2] T. M. Buzug, 'Computed Tomography: From photon statistics to modern cone-beam CT', Berlin Heidelberg: Springer, 2008.

[3] H. Strecker, 'Scatter imaging of aluminum castings using an X-ray fan beam and a pinhole camera', Materials Evaluation, Vol 40, pp 1050-1056, 1982.

[4] G. Harding and E. Harding, 'Compton scatter imaging: A tool for historical exploration', Appl. Radiat. Isotopes, Vol 68, pp 993-1005, 2010.

[5] C. Joseph, 'X-ray backscatter imaging: photography through barriers', Powder Diffr., Vol 21, pp 132-135, 2006.

[6] R. D. Swift, 'Mobile X-ray backscatter imaging system for inspection of vehicles', In: O. L. Malotky, J. J. Pennella, editors, Proceedings of SPIE, Physics-based technologies for the detection of contraband, Vol 2936, pp 124-132, Boston, 1997.

[7] K. Osterloh, U. Zscherpel, M. Jechow, D. Fratzscher, N. Wrobel, and U. Ewert, 'X-ray backscatter imaging with a novel twisted slit collimator', Proceedings of 10th European Conference on Nondestructive Testing (ECNDT), Moscow, Russia, pp 1-8, 2010.

[8] S. Kolkoori, N. Wrobel, K. Osterloh, U. Zscherpel, and U. Ewert, 'Novel X-ray backscatter technique for detection of dangerous materials: Application to aviation and port security', J. Instrum., Vol 8, pp 1-18, 2013.

[9] S. Kolkoori, N. Wrobel, U. Zscherpel, and U. Ewert, 'A new X-ray backscatter imaging technique for non-destructive testing of aerospace materials', NDT&E International, Vol 70, pp 41-52, 2015.

[10] S. Abdul-Majid and A. Balamesh, 'Single side imaging of corrosion under insulation using single photon gamma backscattering', Res. Nondestruct. Eval. Vol 25, pp 172-185, 2014.

[11] W. Niemann and V. Zahorodny, ,Status and future aspects of X-ray backscatter imaging', In: D. O. Thompson, D. E. Chimenti, editors, Review of progress in quantitative non-destructive evaluation, Vol 17. New York, Plenum Press, pp 376-385, 1998.

[12] G. Harding, 'Inelastic photon scattering: Effects and its applications in biomedical science and industry', Radiat. Phys. Chem., Vol 50, pp 91-111, 1997.

[13] G. Harding, 'X-ray scatter tomography for explosives detection', Radiat. Phys. Chem., Vol 71, pp 869-881, 2004.

[14] V. Rebuffel, J. Tabary, and J. Rheinlaender, 'A software simulation tool dedicated to the design and evaluation of X-ray backscatter systems', Proceedings of European Conference on Nondestructive Testing (ECNDT), 2010.

[15] Y. Ham, C. Poranski, and E. Greenawald, 'Monte carlo simulation of X-ray backscatter tomography using visual methods', DGZfP Berichband Vol 44, pp 346-353, 1994.

[16] G. Harding, 'Inelastic photon scattering: effects and applications in biomedical science and industry', Radiation Physics and Chemistry, Vol 50, No. 1, 1997.

[17] J. Gray, T. Aljundi, and A. Turnbull, 'Optimizing Compton backscattering parameters using a simulation code', In: D. O. Thompson, D. E. Chimenti, editors, Review of progress in quantitative non-destructive evaluation, Vol 14, pp 369-376, 1995.

[18] G.-R. Jaenisch, C. Bellon, U. Samadurau, M. Zhukovskiy, and S. Podoliako, 'McRay - A Monte Carlo Model Coupled to CAD for Radiation Techniques', 9th European Conference on NDT 103-CD, pp 1-8, 2006, European Federation for Non-Destructive Testing, ISBN 3-931381-86-2

[19] G.-R. Jaenisch, C. Bellon, U. Samadurau, M. Zhukovskiy, and S. Podoliako, 'Monte Carlo radiographic model with CAD-based geometry description', Insight, Vol 48, No. 10, pp 618-623, 2006.

[20] C. Bellon, A. Deresch, Ch. Gollwitzer, and G.-R. Jaenisch, 'Radiographic simulator aRTist: version 2', 18th WCNDT - World conference on nondestructive testing (Proceedings), pp 1-7 (Paper 333), 2012.

[21] C. Bellon and G.-R. Jaenisch, 'aRTist - Analytical RT Inspection Simulation Tool', DIR 2007 - International Symposium on Digital Industrial Radiology and Computed Tomography (Proceedings), pp 1-5, 2007.

[22] K. Osterloh, U. Ewert, and H. J. Knischek, 'Blende für eine bildgebende Einrichtung', Patent DE 10 2005 029 674, granted 21st August 2008 (in German).

[23] http://www.vision-in-x.com/en/isee-professional.html

[24] A. Deresch, C. Bellon, and G.-R. Jaenisch, 'A general spectrum model for X-ray generators', NDT & E International, Vol 79, pp 92-97, 2016.